Received: 18 November 2024 | Revised: 11 February 2025 | Accepted: 20 February 2025

DOI: 10.1111/jace.20501

Journal of the American Ceramic Society

RESEARCH ARTICLE

Erbium aluminum perovskite ceramics with superior plasma etching resistance

Christian Stern[1,2] | **Doris Sebold**[1] | **Yoo Jung Sohn**[1] | **Martin Bram**[1] | **Olivier Guillon**[1,2,3]

[1]Institute of Energy Materials and Devices (IMD-2), Forschungszentrum Jülich GmbH, Jülich, Germany

[2]Institute of Mineral Engineering, RWTH Aachen University, Aachen, Germany

[3]Jülich Aachen Research Alliance, JARA-Energy, Jülich, Germany

Correspondence
Christian Stern, Institute of Energy Materials and Devices (IMD-2), Forschungszentrum Jülich GmbH, 52425, Jülich, Germany.
Email: c.stern@fz-juelich.de

Abstract

In semiconductor industry, the ongoing miniaturization of the integrated functions on silicon wafers requires the application of harsher plasma compositions during dry etching. At the same time the requirements for cleanliness and wafer-to-wafer reproducibility increase. As a consequence, the erosion of inner wall materials releasing impurity particles into the plasma etching chamber poses a major challenge in semiconductor manufacturing. To mitigate maintenance costs and avoid wafer contamination, conventional materials such as quartz glass (SiO_2) and alumina (Al_2O_3) are gradually exchanged for materials with superior etch resistance. Recently, yttrium aluminum garnet (YAG, $Y_3Al_5O_{12}$) and alternative materials with garnet structure have emerged as promising candidates for this application. In the present study, erbium aluminum perovskite ($ErAlO_3$) was identified as a novel candidate for inner wall materials surpassing the etch resistance of erbium aluminum garnet (ErAG, $Er_3Al_5O_{12}$) and YAG, which were tested as reference materials in the same etch run. Reactive spark plasma sintering (RSPS) was employed for the synthesis of all specimen, which were then exposed to fluorine-based etching plasma. The erosion was characterized using scanning electron microscopy (SEM), energy-dispersive spectroscopy (EDS), and laser scanning microcopy.

KEYWORDS

erbium/erbium compounds, etchants/etching, rare earths, reaction sintering, spark plasma sintering

1 | INTRODUCTION

Ever since its declaration in 1965, semiconductor industry kept Moore's law alive by putting more and more effort into further refinement of the semiconductor manufacturing process. This complex process can be broken down into three different steps: patterning, etching, and doping. Owing to its higher resolution, dry etching, which involves the application of a plasma on the wafer, is the predominant etching technique since the 1970s.[1–5] Driven by the need for the implementation of new material systems with higher plasma resistance, conventional materials such as quartz glass (SiO_2) and alumina (Al_2O_3), which are prone to particulate erosion inducing wafer contamination, are

gradually replaced as component material in plasma etching chambers.[6,7] Due to its higher formation enthalpy and more stable reaction products, yttria (Y_2O_3) has been successfully employed in this kind of application.[8–12] More recently yttrium aluminum garnet (YAG, $Y_3Al_5O_{12}$) has emerged as a cost-efficient alternative with comparable plasma etching resistance.[13] In our previous study aiming on enhanced etch resistance, alternative garnets, where the yttrium ion in the garnet crystal was replaced with the heavier lanthanoids Er and Lu, exhibited comparable etch resistance as YAG.[14]

The interaction of the Al_2O_3–Y_2O_3 system with fluorine-based etching plasma has been excessively studied in the past. Tan et al.[15] suggest that the etch resistance increases with increasing Y_2O_3 content and follows a percolation transition. Further research has been carried out on the etch resistance of the compounds of the Al_2O_3–Y_2O_3 system with the intermediate phases being YAG, yttrium aluminum perovskite (YAP, $YAlO_3$), and yttrium aluminum monoclinic (YAM, $Y_4Al_2O_9$).[16] The results show that the intermediate phases have a significantly better plasma etch resistance than alumina and that when comparing the etch rates of YAG, YAP, and YAM, intermediate phases with higher yttria portion have a slightly better etch performance. Furthermore, the etch performance of pure yttria slightly outperforms the intermediate phases.[17–19] However, the difference in etch rates is small and depending on the plasma gas composition and experimental parameters.[7]

Based on the encouraging results on the etch performance of a phase pure erbium aluminum garnet (ErAG) sample in our most recent work,[14] this study focuses on the etch performance of the Er_2O_3–Al_2O_3 system. Therefore, two samples were processed. One sample is leaning toward erbia excess from the stoichiometric composition of ErAG ($Er_3Al_5O_{12}$) resulting in a dual phase material containing $ErAlO_3$ (ErAP) as secondary phase homogeneously distributed in an ErAG matrix. This samples enables a direct comparison of the etch resistance of both phases in the immediate neighborhood. To our understanding such direct comparison is necessary since there is a certain deviation of the etch attack depending on the etch run and the position of the sample in the plasma chamber.[14] The second sample consists of the pure ErAP phase enabling a direct comparison to pure ErAG, pure YAG, and our usual quartz glass reference. Because our previous study showed the negative impact of alumina phase on the plasma etch resistance, the alumina rich portion of the phase diagram was not considered for this study.

All ceramic samples investigated in this study were processed by reactive spark plasma sintering (RSPS) and subsequently exposed to a fluorine-based etching plasma together with the above-mentioned reference materials. Fluorocarbon plasmas are commonly employed in dry etching processes owing to the high selectivity between silicon (Si) and silicon dioxide (SiO_2).[20–23] The plasma erosion was characterized with scanning electron microscopy (SEM)/energy-dispersive spectroscopy (EDS) and confocal laser scanning microscopy. Our results indicate that ErAP features superior etch performance than both YAG and ErAG.

2 | EXPERIMENTAL PROCEDURE

In this study, RSPS was employed for synthesizing erbium aluminates. This technique has been successfully applied for the synthesis of YAG and alternative garnets before.[14,24] High-purity commercial alumina (A1 grade, 99.999%, d_{50} = 1.1 μm, Heraeus Holding GmbH), yttria (99.999% purity, d_{50} = 6.0 μm, Neo Performance Materials Inc.), and erbia (99.99% purity, d_{50} = 7.6 μm, Neo Performance Materials Inc.) were used as raw materials. The particle size distribution (PSD) of these materials was measured using a LA950 V2 particle size analyzer (Horiba), with the results summarized in Figure S1. Before the sintering step, the morphology of the powder blend was examined using SEM(Ultra 55, Carl Zeiss AG). The results confirm the PSD and show large chunks of Er_2O_3, that are covered with finer Al_2O_3. Exemplary SEM images can be found in Figure S2. Additionally, the materials were characterized by X-ray diffraction (XRD; D4 Endeavor, Bruker, 10°–140° in 2θ range, increment 0.02°, 0.75 s/step).

For the synthesis of the ErAG/ErAP composite and the single phase ErAP sample, two powder blends containing 40 and 50 mol% Er_2O_3 were processed. Theses compositions were chosen with respect to the Er_2O_3–Al_2O_3 phase diagram, which is given in Figure S3. In the first blend, the erbia portion is slightly exceeding the stoichiometric composition of ErAG (37.5 mol% Er_2O_3), which suggests a microstructure predominantly composed of ErAG with ErAP as a secondary phase. The second blend, containing equal amounts of erbia and alumina, corresponds to the stoichiometric composition of ErAP.[25] By examining both ErAP as a secondary phase and as the main phase, we aim to verify the results on the plasma etch resistance. For the synthesis of the YAG reference sample, alumina and yttria were weighed according to the stoichiometric ratio: 37.5 mol% yttria and 62.5 mol% alumina.[16] By adding alumina grinding balls (Ø 10 mm) and ethanol as solvent, a slurry was formed and then homogenized in polyethylene (PE) bottles for 24 h on a roller bench. The potential impact of grinding ball abrasion on the stoichiometry was not considered. The slurry was subsequently dried using a rotary evaporator. Before sintering, the dried powder was sieved

TABLE 1 Plasma parameters applied for plasma etching experiments.

P_{ICP} (W)	t_{etch} (min)	p (mbar)	U_B (V)	CF_4 (sccm)	Ar (sccm)	O_2 (sccm)
600	120	0.01	−250	1.0	5.0	0.5

through a 90 µm mesh, calcined at 1000°C for 3.5 h, and then sieved again through a 90 µm mesh.

For the synthesis, a spark plasma sintering apparatus (HP D5, FCT Systeme GmbH) was used to compact cylinders with a diameter of 20 mm and a height of approximately 3 mm, employing graphite dies as the tool material. While reactive sintering of YAG is described in detail in the literature, information on the reactions of Al_2O_3 and Er_2O_3 is sparse. Therefore, sintering parameters to achieve desirable conversion to ErAP were derived from literature on the interaction of yttria and alumina.[26,27]

Following an initial precompaction at 20 MPa, the samples underwent heating at a rate of 25 K/min until reaching 1000°C, with simultaneous application of a uniaxial pressure of 5 MPa. In the following heating step the heating rate was reduced to 10 K/min, while the pressure was increased to 25 MPa. After reaching 1450°C for the perovskite phase and 1625°C for the garnet samples, respectively, the samples dwelled for a duration of 30 min under a constant pressure of 25 MPa. Afterward, the system was switched to active cooling mode.

For conducting etch experiments, the samples were cut into 10 mm × 10 mm squares and the thickness was reduced to less than 1 mm through a series of grinding and polishing steps. The final polishing was performed with colloidal silica to achieve a smooth, mirror-like surface and thereby remove any defects that could affect the erosion process. Prior to plasma exposure, each sample was partially covered with plasma-resistant polyimide (Kapton®) tape, leading to the formation of etch steps, which were used to assess the etch rate.

For the experiments an inductively coupled plasma (ICP) reactor was used, and a mixture of CF_4, Ar, and O_2 was employed as plasma gas, with CF_4 being the chemically reactive species and Ar the physically reactive species. O_2 was added to prevent the formation of a polymer layer.[28,29] A detailed description of the experimental setup and the working principle of the etch chamber are available in the literature.[30] The parameters that were used for the etch trail are shown in Table 1.

After removing the plasma-resistant Kapton® tape, the resulting surface topography was examined using confocal laser scanning microscopy (VK-9710, Keyence Corporation). Furthermore, SEM (Gemini 450, Carl Zeiss AG) was employed for the characterization of the microstructure before and after plasma exposure.

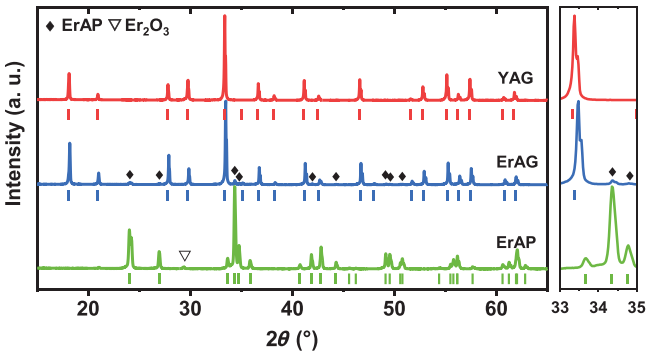

FIGURE 1 X-ray diffraction (XRD) pattern of yttrium aluminum garnet (YAG), erbium aluminum garnet (ErAG), and erbium aluminum perovskite (ErAP). The enlarged section on right side shows the 100% peaks.

3 | RESULTS AND DISCUSSION

Figure 1 compares the XRD patterns in the as sintered state, with the 100% peaks in the enlarged section on the right-hand side. All peaks are assigned to the respective phases, and the main phase is marked with dashes of the same color below each pattern. In the YAG sample no secondary phase was detected, whereas the enlarged pattern of the ErAG sample clearly features the aspired ErAP as a secondary phase. Contrarily, in the ErAP sample still a small amount of erbia was detected as a secondary phase, which will be considered in the discussion of the etching results later. For a deeper understanding of the phase composition Rietveld refinements of the measured XRD patterns of ErAG and ErAP were carried out using the software package Topas 4.2.[31] The ErAG–ErAP composite consists of 93% garnet and 7% perovskite phase and the ErAP sample contains 1% residual erbia. The results are also given as Figures S4 and S5.

The corresponding backscattered electron (BSE)-SEM images to the XRD patterns are shown in Figure 2 and were taken with an acceleration voltage of 8.0 kV. In the ErAP sample (Figure 2A) small amounts of the brighter Er_2O_3 secondary phase, indicated by green arrows, are visible. The bright contrast of Er_2O_3 can be attributed to its larger average atomic number compared to the ErAP matrix. It is also apparent that the grain boundaries contain flaws due to microcracks, which may lead to grains becoming loose and causing outbreaks. In the SEM image of ErAG (Figure 2B), the brighter ErAP secondary phase can clearly be seen. The brighter contrast of the ErAP phase can be explained by the higher average atomic number of the compound. An additional EDS mapping that confirms the presence of ErAP as a secondary phase can be found in Figure S6. The third SEM image of the YAG sample (Figure 2C) shows a

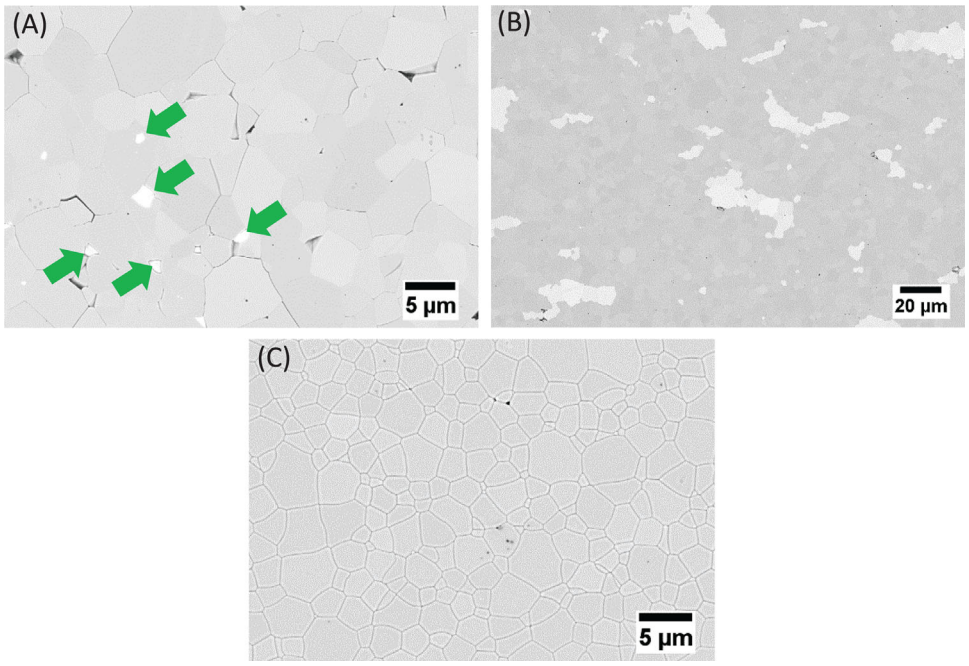

FIGURE 2 Backscattered electron (BSE)-scanning electron microscopy (SEM) of as sintered samples. (A) Erbium aluminum perovskite (ErAP), green arrows indicate residual Er_2O_3, (B) erbium aluminum garnet (ErAG)/ErAP composite, (C) yttrium aluminum garnet (YAG).

TABLE 2 Relative density of specimen processed in this work.

Material	Rel. density (%)
Yttrium aluminum garnet (YAG)	99.1
Erbium aluminum garnet (ErAG)/erbium aluminum perovskite (ErAP) composite	99.8
ErAP	98.4

homogenous, single-phased microstructure. In order to make grain boundaries visible, this sample was thermally etched at 1250°C for 30 min. Generally speaking, all samples were consolidated close to the theoretical density with no pores visible in SEM. To confirm this, the relative density of the samples was determined according to the Archimedes principle, with the results shown in Table 2. All samples have a relative density of more than 98%, which can be attributed to the spark plasma sintering (SPS) approach. The absence of pores is crucial in plasma etching, as residual porosity gets preferentially eroded during plasma exposure.

To determine the erosion depth after plasma etching, four topography line scans of the etch step, evenly distributed along it, were averaged. The procedure that leads to the topography of the etch step as well as an exemplary line-scan showing the resulting topography are provided in Figure S7. The determined erosion depths are summarized in Figure 3. The outcome indicates that the erosion depth in the ceramic samples is more than an order of

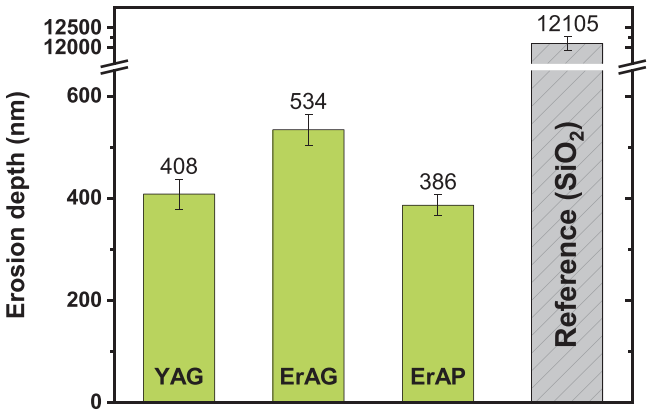

FIGURE 3 Erosion depth determined with the confocal laser scanning microscope.

magnitude smaller compared to the quartz glass reference, which underlines the excellent etch resistance of all three materials. Among the ceramic samples, the ErAP sample exhibits the smallest erosion depth, while YAG performs on a similar level but got slightly more eroded. The ErAG sample was eroded about 125 nm more compared to YAG. The derived erosion rates are 204 nm/h for YAG, 267 nm/h for ErAG, 193 nm/h for ErAP and 6.05 µm/h for the quartz glass reference respectively.

The corresponding SEM images (Figure 4A,B) of the surface of ErAP after plasma exposure, taken at an acceleration voltage of 8.0 kV, show significant marks of heavy physical damage. On the one hand sputtering craters that

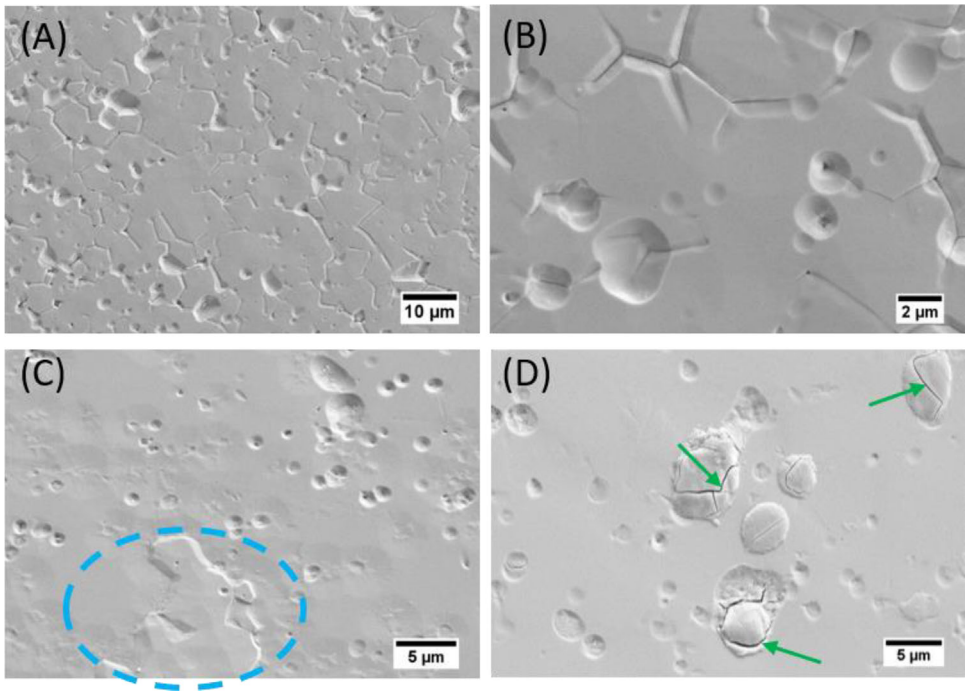

FIGURE 4 Secondary electron (SE)-scanning electron microscopy (SEM) of etched surface. (A, B) Erbium aluminum perovskite (ErAP); (C) erbium aluminum garnet (ErAG) with ErAP secondary phase (blue dashed line); (D) yttrium aluminum garnet (YAG) with reaction products.

tend to form at grain boundaries and triple points are apparent. On the other hand, the grain boundaries were preferentially eroded by the plasma, likely due to the presence of microcracks (see Figure 2A). These microcracks facilitated localized erosion along the grain boundaries, resulting in a topography of scattered deep sputtering craters and trenches along parts of the grain boundaries. Physical damage is also apparent in the SEM images of the garnet samples; however, here different erosion mechanisms are apparent. Preferentially eroded grain boundaries were not observed (Figure 4C,D) but randomly distributed sputtering craters were found on both garnet samples. At the same time, the less eroded ErAP secondary phase can be observed in the nonstoichiometric ErAG sample (Figure 4C, marked with blue dashed line). Less eroded regions were also observed on the YAG sample (Figure 4D). The corresponding EDS analysis is given in Figure S8 and shows that these areas have higher C and F signals compared to the surrounding. Therefore, we conclude that these areas formed due to reactions with the fluorine-based etching plasma. Visible cracks (green arrows in Figure 4D) suggest that these products grow during etching and fall of at some point due to physical damage caused by Ar^+ sputtering.

Figure 5 shows the topography at the etch step in the dual-phased ErAG sample analyzed with the laser microscope. The lower half of the sample was protected from the plasma by the Kapton tape and therefore not eroded. The upper half however was exposed to the plasma, resulting in physical erosion. Within the etched surface, the significantly less eroded ErAP phase is visible. Further analysis of the topography with a line scan (Figure 5 red arrow) revealed that the ErAP secondary phase was eroded about 150–160 nm less than the ErAG matrix. This result is in excellent agreement with the determined erosion depth of the whole samples (Figure 3), where the ErAP sample was eroded about 150 nm less than ErAG and underlines the superior plasma etching resistance of ErAP over ErAG. Topographic images of the etch step in ErAP and YAG are provided in Figures S9 and S10, respectively.

4 | CONCLUSIONS

In this study, ceramic samples with garnet and perovskite structures were successfully synthesized using RSPS. While the YAG reference exhibited no secondary phase, the ErAP sample contained small amounts of Er_2O_3. The composition of the ErAG sample was intentionally leaning toward Er_2O_3 excess, resulting in the formation of ErAP as a secondary phase. The microstructure of the sintered YAG and ErAG samples is dense and homogenous, except for the secondary phase in ErAG. In the perovskite sample, the grain boundaries present flaws. In the corresponding SEM images microcracks between

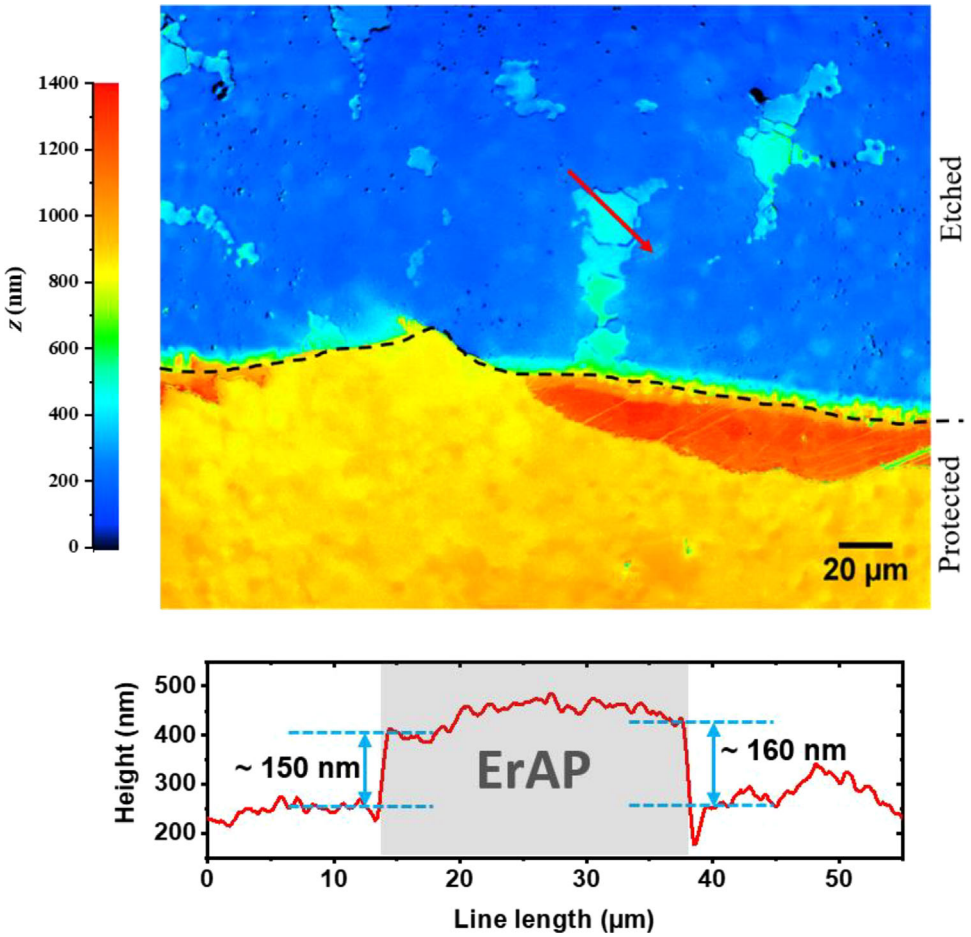

FIGURE 5 Topography at the etch step in dual-phased erbium aluminum garnet (ErAG) with erbium aluminum perovskite (ErAP) secondary phase. Image taken with the laser microscope. Topography line scan illustrates different erosion of ErAG matrix and ErAP secondary phase.

grains, which could eventually lead to material outbreaks, are clearly visible. This indicates the potential for further optimization of the sintering parameters and processing route.

Following plasma exposure, the resulting erosion depth was determined using the laser scanning microscope. The results demonstrate the superior plasma resistance of the ErAP phase compared to the YAG reference, while the ErAG coupon exhibited more erosion than the reference. Nevertheless, compared to the quartz glass reference, all materials feature an excellent etch resistance. Additionally, SEM analysis revealed significant physical damage on the surface of the plasma-exposed samples. On the YAG and ErAG samples, randomly distributed sputtering craters were found. The SEM images of the nonstoichiometric ErAG sample also indicate that the ErAP secondary phase was less eroded than the ErAG matrix, highlighting the superior etch resistance of this phase. On the YAG sample, reaction products with the fluorine-based etching plasma were found. SEM images of the ErAP sample revealed sputtering craters and preferentially eroded grain boundaries, which is consistent with the presence of microcracks found prior to plasma etching.

Our results suggest that analogous to the Y_2O_3–Al_2O_3 system, the etch resistance in the Er_2O_3–Al_2O_3 system increases with decreasing alumina content. An impact of the small amount of residual erbia in the ErAP sample on the erosion process was not obvious. However, to reliably benchmark the two systems, samples with equivalent erbia and yttria content must be etched in the same trial.

The discovery of the ErAP phase as a highly etch-resistant material is particularly significant, as it provides a promising alternative to conventional etch-resistant ceramics. Its enhanced resistance to plasma erosion compared to YAG suggests potential applications in environments where minimizing material degradation is critical, such as in semiconductor processing or protective coatings for plasma-facing components. This finding broadens the material selection for advanced plasma-resistant ceramics, making ErAP a strong candidate for future research and industrial applications. Moreover, investigations of alternative lanthanoid aluminates beyond erbium could result

in valuable insights. According to the existing literature, the R_2O_3–Al_2O_3 systems (R = Pm, Sm, Eu, Gd, Tb, Dy, Ho, Er, Tm) feature both (meta)stable garnet and perovskite phases, suggesting potential routes for further research.[25]

ACKNOWLEDGMENTS

The authors acknowledge Elia Jüngling (Ruhr University Bochum) for performing plasma etching experiments.

Open access funding enabled and organized by Projekt DEAL.

ORCID

Christian Stern https://orcid.org/0009-0002-7254-5248
Yoo Jung Sohn https://orcid.org/0000-0002-7994-7269
Olivier Guillon https://orcid.org/0000-0003-4831-5725

REFERENCES

1. Pearton SJ, Norton DP. Dry etching of electronic oxides, polymers, and semiconductors. Plasma Processes Polym. 2004;2(1):16–37. https://doi.org/10.1002/ppap.200400035
2. Nojiri K. Dry etching technology for semiconductors. Switzerland: Springer International Publishing; 2015. https://doi.org/10.1007/978-3-319-10295-5
3. Mack C. Fundamental principles of optical lithography: the science of microfabrication. Chichester, England: John Wiley & Sons; 2007. https://doi.org/10.1002/9780470723876
4. Moore G. Cramming more components onto integrated circuits. Electronics. 1965;38(8):114–17. https://doi.org/10.1109/JPROC.1998.658762
5. Eeckhout L. Is Moore's law slowing down? What's next? IEEE Micro. 2017;37(4):4–5. https://doi.org/10.1109/MM.2017.3211123
6. Ashizawa H, Yoshida K. Effect of the microstructures of yttria ceramics on their plasma corrosion behavior. Ceram Int. 2019;45(17):21162–67. https://doi.org/10.1016/j.ceramint.2019.07.093
7. Ma HJ, Hong S, Oh HM, Kumar K, Kim MJ, Kim HN, et al. Correlation with the microstructure and synergistic physiochemical etching resistance of nanocomposites under fluorine-containing plasma conditions. ACS Appl Mater Interfaces. 2022;14(38):43771–82. https://doi.org/10.1021/acsami.2c12311
8. Miwa K, Sawai T, Aoyama M, Inoue F, Oikawa A, Imaoka K. Particle reduction using Y_2O_3 material in an etching tool. Paper presented at: 2007 international symposium on semiconductor manufacturing; 15–17 October 2007; Santa Clara, CA, USA. https://doi.org/10.1109/ISSM.2007.4446866
9. Kim D-M, Oh Y-S, Kim S, Kim H-T, Lim D-S, Lee S-M. The erosion behaviors of Y_2O_3 and YF_3 coatings under fluorocarbon plasma. Thin Solid Films. 2011;519(20):6698–702. https://doi.org/10.1016/j.tsf.2011.04.049
10. Park SH, Kim KE, Hong SJ. Surface analysis of chamber coating materials exposed to CF_4/O_2 plasma. Coatings.2021; 11(1):105. https://doi.org/10.3390/coatings11010105
11. Ma HJ, Kim S, Kim HN, Kim MJ, Ko JW, Lee JW, et al. Microstructural characterization and inductively coupled plasma-reactive ion etching resistance of Y(2)O(3)-Y(4)Al(2)O(9) composite under CF(4)/Ar/O(2) mixed gas conditions. Sci Rep. 2024;14(1):7008. https://doi.org/10.1038/s41598-024-57697-5
12. Ashizawa H, Masakatsu K, Yoshida K. Microstructure and plasma corrosion behavior of yttria coatings prepared by the aerosol deposition method. J Am Ceram Soc. 2020;103(12):7031–40. https://doi.org/10.1111/jace.17193
13. Mitsuhiro Fujita KM. Plasma-resistant member for semiconductor manufacturing apparatus and method for manufacturing the same. U.S. Patent No. 6,838,405. 2005.
14. Stern C, Schwab C, Kindelmann M, Stamminger M, Weirich TE, Park I, et al. Correlative characterization of plasma etching resistance of various aluminum garnets. J Am Ceram Soc. 2024;107(11):7105–18. https://doi.org/10.1111/jace.19951
15. Tan Y, Chen P, Zhu Z, Wu S, Tian Z. Plasma etching behavior of yttrium-aluminum oxide composite ceramics. Int J Appl Ceram Technol. 2021;18(5):1710–15. https://doi.org/10.1111/ijac.13712
16. Cockayne B. The uses and enigmas of the Al_2O_3-Y_2O_3 phase system. J Less Common Met. 1985;114(1):199–206. https://doi.org/10.1016/0022-5088(85)90402-3
17. Kim D-M, Lee S-H, Alexander WB, Kim K-B, Oh Y-S, Lee S-M. X-ray photoelectron spectroscopy study on the interaction of yttrium-aluminum oxide with fluorine-based plasma. J Am Ceram Soc. 2011;94(10):3455–59. https://doi.org/10.1111/j.1551-2916.2011.04589.x
18. Qin X, Zhou G, Yang H, Wong JI, Zhang J, Luo D, et al. Fabrication and plasma resistance properties of transparent YAG ceramics. Ceram Int. 2012;38(3):2529–35. https://doi.org/10.1016/j.ceramint.2011.11.023
19. Kim E-B, Zhao C-C, Park Y-J, Kim M-J, Ma H-J, Kim H-N, et al. Effect of porosity on etching rate and crater-like microstructure of sintered Al_2O_3, Y_2O_3, and YAG ceramics in plasma etching. Ceram Int. 2024;50(9):15182–94. https://doi.org/10.1016/j.ceramint.2024.01.436
20. Cardinaud C. Fluorine-based plasmas: main features and application in micro- and nanotechnology and in surface treatment. CR Chim 2018;21(8):723–39. https://doi.org/10.1016/j.crci.2018.01.009
21. Cardinaud C, Peignon M-C, Tessier P-Y. Plasma etching: principles, mechanisms, application to micro- and nanotechnologies. Appl Surf Sci. 2000;164(1-4):72–83. https://doi.org/10.1016/S0169-4332(00)00328-7
22. Donnelly VM, Kornblit A. Plasma etching: yesterday, today, and tomorrow. J Vacuum Sci Technol A: Vacuum Surf Films. 2013;31(5):050825. https://doi.org/10.1116/1.4819316
23. Butterbaugh JW, Gray DC, Sawin HH. Plasma–surface interactions in fluorocarbon etching of silicon dioxide. J Vac Sci Technol B. 1991;9(3):1461–70. https://doi.org/10.1116/1.585451
24. Wang P, Huang Z, Morita K, Li Q, Yang M, Zhang S, et al. Influence of spark plasma sintering conditions on microstructure, carbon contamination, and transmittance of CaF_2 ceramics. J Eur Ceram Soc. 2022;42(1):245–57. https://doi.org/10.1016/j.jeurceramsoc.2021.10.004
25. Wu P, Pelton AD. Coupled thermodynamic-phase diagram assessment of the rare earth oxide-aluminium oxide binary systems. J Alloys Compd. 1992;179(1-2):259–87. https://doi.org/10.1016/0925-8388(92)90227-Z
26. Glushkova VB, Krzhizhanovskaya VA, Egorova ON, Udalov YP, Kachalova LP. Reaction of yttrium and aluminum oxides. Chemischer Informationsdienst. 1983;14(21):80–84.

27. Caslavsky JL, Viechnicki DJ. Melting behaviour and metastability of yttrium aluminium garnet (YAG) and $YAlO_3$ determined by optical differential thermal analysis. J Mater Sci. 1980;15(7):1709–18. https://doi.org/10.1007/BF00550589
28. Mogab CJ, Adams AC, Flamm DL. Plasma etching of Si and SiO_2—the effect of oxygen additions to CF_4 plasmas. J Appl Phys. 1978;49(7):3796–803. https://doi.org/10.1063/1.325382
29. Reid I, Hughes G. Influence of plasma parameters on the chemical composition of steady-state fluorocarbon films deposited on carbon-doped low-k dielectric layers during etching. Semicond Sci Technol. 2006;21(9):1354–57. https://doi.org/10.1088/0268-1242/21/9/023
30. Stamminger M. Fluorocarbon plasma erosion of silica glass doped with aluminum. Bochum: Ruhr University Bochum; 2020. https://doi.org/10.13154/294-6890
31. Bruker AXS. TOPAS V4: general profile and structure analysis software for powder diffraction data. Karlsruhe, Germany: Bruker AXS; 2008.

SUPPORTING INFORMATION

Additional supporting information can be found online in the Supporting Information section at the end of this article.

How to cite this article: Stern C, Sebold D, Sohn YJ, Bram M, Guillon O. Erbium aluminum perovskite ceramics with superior plasma etching resistance. J Am Ceram Soc. 2025;108:e20501. https://doi.org/10.1111/jace.20501